Design and identification of high performance steel alloys for structures subjected to underwater impulsive loading

Felix Latourte [a], Xiaoding Wei [a], Zechariah D. Feinberg [b], Alban de Vaucorbeil [a], Phuong Tran [a], Gregory B. Olson [b], Horacio D. Espinosa [a,*]

[a] Dept. of Mechanical Engineering, Northwestern University, 2145 Sheridan Road, Evanston, IL 60208-3111, USA
[b] Dept. of Material Science, Northwestern University, 2220 Campus Drive, Evanston, IL 60208-3108, USA

ARTICLE INFO

ABSTRACT

Martensitic and austenitic steel alloys were designed to optimize the performance of structures subjected to impulsive loads. The deformation and fracture characteristics of the designed steel alloys were investigated experimentally and computationally. The experiments were based on an instrumented fluid–structure interaction apparatus, in which deflection profiles are recorded using a shadow Moiré technique combined with high speed imaging. Fractographic analysis and post-mortem thickness reduction measurements were also conducted in order to identify deformation and fracture modes. The computational study was based on a modified Gurson damage model able to accurately describe ductile failure under various loading paths. The model was calibrated for two high performance martensitic steels (HSLA-100 and BA-160) and an austenitic steel (TRIP-120). The martensitic steel (BA-160) was designed to maximize strength and fracture toughness while the austenitic steel (TRIP-120) was designed to maximize uniform ductility, in other words, to delay necking instability. The combined experimental–computational approach provided insight into the relationships between material properties (strength, uniform ductility, and post-necking ductility) and blast resistance of structures. In particular, the approach allowed identification of material/structure performances by identifying impulse-center deflection behavior and the impulse leading to panel fracture.

1. Introduction

Dynamic transverse loading of circular plates has been studied by several investigators and closed form solutions derived to describe plate deflection when subjected to underwater explosions (Cole, 1948; Jones, 1989; Taylor, 1963; Wierzbicky, 1969; Wojno and Wierzbicki, 1980). Recent reviews described available theoretical predictions of the response of loaded plates, accounting for fluid–structure interaction, strain rate effects and energy partition associated to these dynamic events (Nurick and Martin, 1989a,b; Rajendran and Narasimhan, 2006). From these studies, it emerges that performance improvements can be achieved through material optimization (improved strength, hardening rate, uniform ductility, and failure strain). In fact, for a given applied impulse, maximum panel center deflection is inversely proportional to material yield strength. Likewise, uniform ductility controls the onset of necking, which is a precursor to fracture. Hence, high strength materials capable of delaying necking instability are very desirable.

In addition to material improvements, topological structural optimization can also lead to major improvements in performance. For instance, sandwich structures with various core topologies have been investigated to assess the benefits arising from fluid–structure interaction effects (Deshpande and Fleck, 2005; Latourte et al., 2011; Hutchinson and Xue, 2005; Liang et al., 2007; Mori et al., 2007, 2009; Qiu et al., 2004; Vaziri et al., 2007; Xue and Hutchinson, 2003). These studies showed that the performance of sandwich structures is governed by core topology, mass distribution between core and facesheets, and by constitutive material behavior.

To characterize the performance of naval structures, air and underwater blast experiments have been developed. Air blast experiments are relatively simple since they only require an explosive and a foam pad to load the sample (Florence, 1966; Neuberger et al., 2007; Nurick et al., 1996). In water blast experiments, the impulse transfer to the specimen is more complex since fluid–structure interaction effects are prominent. Only a few scaled down experimental approaches have been introduced to study the performance of immersed structures loaded impulsively (Espinosa et al., 2006; Qiu et al., 2004), while full scale experiments are seldom and do not typically provide real time monitoring of

---

panel deflection (Rajendran and Narashimhan, 2001). These experimental techniques have revealed that failure of monolithic and sandwich panels include tensile tearing in the central region, transverse shearing failure at the supports, and for certain sandwich panels, facesheet perforation. Hence, optimization of sandwich panel performance is usually achieved by a balance between facesheet integrity on one side, core crushing to enhance the FSI effect, and overall energy absorption capabilities on the other. Likewise, performance of metallic monolithic structures is governed by material strength, uniform and post necking ductility, and hardening and strain rate sensitivity. Therefore, given that materials designed to optimize solid panel performance can also be integrated into the design of sandwich structures, the development of high performance materials can lead to superior combinations of material–structural designs. Such combination was investigated in (Vaziri et al., 2007), where solid panels were numerically compared with sandwich panels, and the influence of the material was examined through different material choices. The study highlighted the trade-off between strength and ductility on panel performance.

Combining strength and ductility is problematic for material designers, but recent advances in material design have been driven by the automotive and naval industries where cost effective, lightweight and resistant structures are desired. In this context, the benefits of the transformation induced plasticity (TRIP) concept have been raised, since the austenite to martensite transformation improves work hardening while maintaining high levels of ductility (Olson, 1996). More generally, new materials where both high strength and ductility are achieved are often designated as advanced high strength steels (AHSS), namely, high strength low alloy precipitation strengthened martensitic steels (HSLA), ferritic–martensitic dual phase steels (DP), and TRIP steels.

This paper deals with the design of different steel alloys and the performance identification of monolithic panels subjected to underwater impulsive loading. We start with a discussion of material design based on deformation modes elicited in structures subjected to blast loading. Then, experimental and computational methodologies, used to investigate material–structural performance when subjected to underwater impulse loading, are described. Results for three steel alloys – the martensitic steel HSLA-100, currently used in naval hulls (Czyryca et al., 1990a; Nichols, 1990), the martensitic steel called blastalloy 160 (BA-160) in (Saha, 2004; Saha et al., 2007; Saha and Olson, 2007), and the fully austenitic TRIP steel called TRIP-120 in (Sadhukhan, 2008) – are presented. Next, a discussion of FSI experimental results and finite element predictions based on an extended Gurson model is provided. The paper closes with a discussion of two approaches to design a novel TRIP steel alloy, which can *simultaneously* achieve high strength, uniform ductility, and failure strains.

2. Material design

2.1. HSLA-100

The high-strength low-alloy steel HSLA-100 was developed by the United States Navy in the early 1990s to reduce fabrication costs in ship construction (Czyryca et al., 1990a,b,c; Nichols, 1990; Sawhill, 1990). In this study, HSLA-100 is used as the reference steel alloy in examining performance improvement. This martensitic steel has similar strength (a yield stress of 100 ksi or 689 MPa) and toughness to the alloy it replaced – HY-100. HSLA-100 was designed with reduced carbon content in order to make it weldable without preheat, which in turn reduces fabrication costs with respect to HY-100. To compensate the reduced carbon content, copper was added to provide an additional precipitation

strengthening mechanism (Das et al., 2006; Dunne et al., 1996; Goodman et al., 1973). Copper precipitates also contribute to an increase in the corrosion resistance (Irvine and Pickering, 1963). HSLA-100 processing entails solutionizing, quenching, and tempering at 620–690 °C to obtain a martensitic steel with dispersed Cu precipitates and alloy carbides (Czyryca et al., 1990a,b,c; Nichols, 1990; Sawhill, 1990).

HSLA-100 has been extensively investigated in the past two decades. Studies have been carried out to optimize heat treatments (Dhua et al., 2003) and also to investigate relationships between strength and microstructure (Vaynman et al., 2008). The mechanical performance of HSLA-100 has been characterized through studies of its fracture behavior (Das et al., 2006; Densley and Hirth, 1998) and its ballistic resistance (Martineau et al., 2004).

The HSLA-100 material characterized in this study was provided by Arcelor Mittal, where a 25.4 mm thick plate was hot rolled from a 230 mm thick slab. A typical heat treatment recipe was provided by Arcelor Mittal consisting of a solution treatment at 900 °C for 31 min followed by a water quench, and then aging at 580 °C for 1 h followed by air cooling.

2.2. Blastalloy 160

Blastalloy 160 (BA-160) was designed and developed at Northwestern University and its design and mechanical performance in term of plastic yield stress and impact energy were presented in (Saha, 2004; Saha et al., 2007; Saha and Olson, 2007). Blastalloy 160 was designed using a systems-based design approach to develop a martensitic steel that would meet the projected naval hull material requirements in the year 2020. Design objectives include high strength (160 ksi yield strength), high impact fracture toughness (C_v >115 J corresponding to K_{Id} >220 MPa m$^{1/2}$), good weldability (C content <0.1 wt.%), and high resistance to hydrogen stress corrosion cracking (K_{ISCC}/K_{IC} >0.5). Computational tools were utilized to design a martensitic steel alloy that could achieve all of these property objectives.

In order to achieve the strength goal with limited carbon content to maintain weldability, BA-160 makes use of two precipitate strengthening contributions – fine dispersions of 3 nm M_2C carbides and BCC copper. Quantitative models have been developed for the strengthening contributions that arise from the fine dispersion of M_2C carbide precipitates (Wise, 1998) and BCC copper precipitates (Russell and Brown, 1972). The M_2C carbide strengthening contribution is limited by the carbon content of 0.05 wt.%, which is the carbon level in the current alloy used by the Navy (HSLA-100). With the carbon content set, the sum of the M_2C carbide formers (Cr, Mo, and V) must be twice the carbon concentration for stoichiometric balance. These M_2C carbides were incorporated into the design to dissolve the cementite in the matrix such that strength and toughness goals were achieved. Finally, the required copper concentration was determined to provide the final strengthening contribution to achieve the strength objective. The final design of BA-160 makes use of three strengthening contributions to achieve the strength goal, as shown in Fig. 1c, the martensitic matrix, the M_2C carbide precipitates, and the BCC copper precipitates. Three-dimensional atom probe work has verified the presence of both M_2C carbides and copper precipitates after optimum tempering as shown by the reconstruction in Fig. 1c.

BA-160 also integrates dispersed austenite into its design to increase toughness. Fine dispersions of stable austenite particles delay microvoid nucleation and the onset of shear localization, which is the primary cause of fracture in ultrahigh strength steels (Haidemenopoulos, 1988). In order to maximize the toughening enhancement of dispersed austenite, it is imperative to control the stability of the austenite particles, which is based on the phase fraction, size, and composition of the precipitated austenite. The
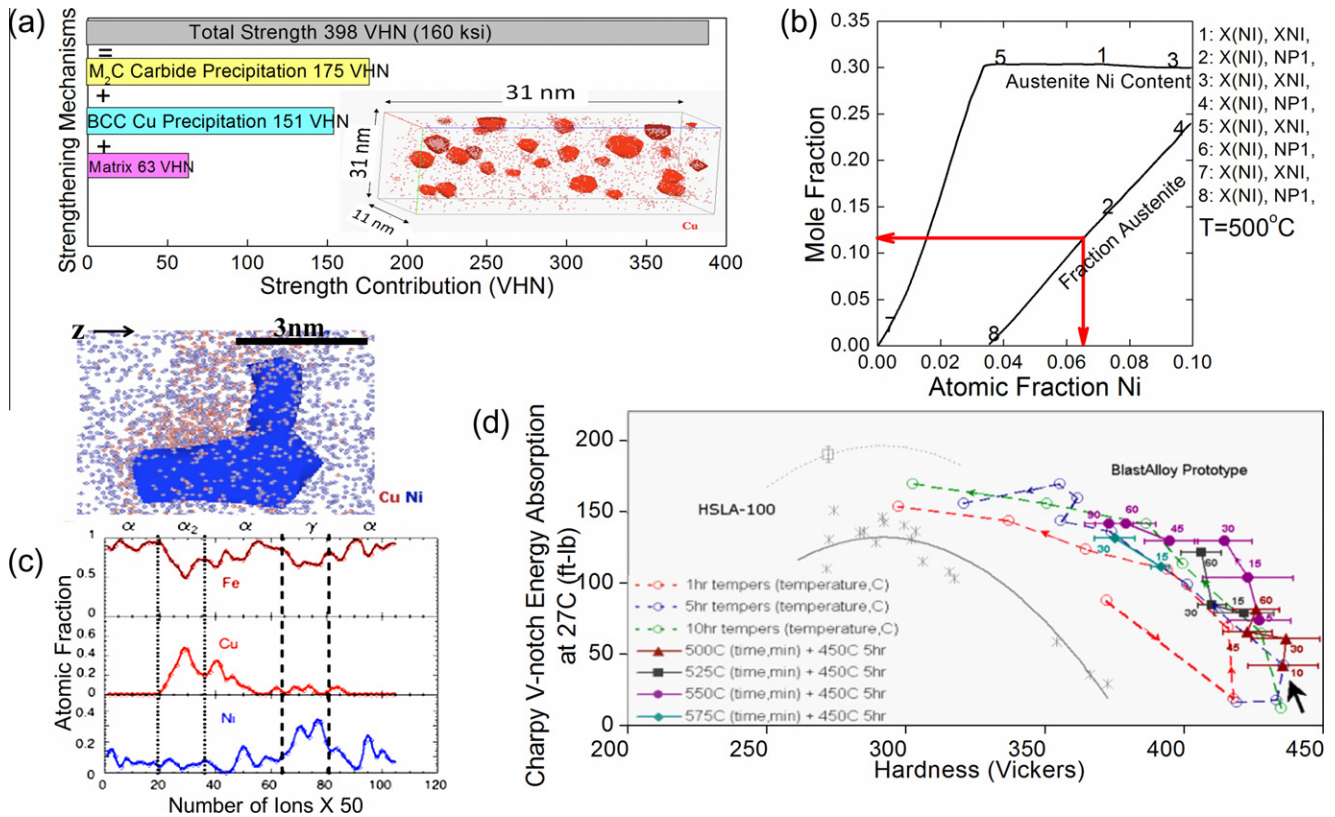
Fig. 1. The design of BA-160 incorporates M_2C carbide precipitates and BCC copper precipitates to achieve the strength goal and also includes dispersed austenite for transformation toughening to meet the desired property objectives. (a) In order to achieve the strength goal of 160 ksi, BA-160 utilizes strengthening contributions of the matrix, BCC Cu precipitates, and M_2C carbide precipitates as confirmed by atom-probe tomography; (b) BA-160 was designed with sufficient Ni content to precipitate out a phase fraction of 10% austenite with the desired stability. An equilibrium calculation using ThermoCalc shows that with 6.5 wt.% Ni, at least 10% austenite phase fraction, is obtained and the precipitated austenite phase will be composed of 30% Ni; (c) an isolated Ni-rich precipitated austenite particle, which contributes to improved fracture toughness, was observed with atom-probe tomography; (d) the design of BA-160 utilizes dual precipitation strengthening and dispersed austenite to achieve high combinations of strength and toughness.

austenite phase fraction and composition was modeled with ThermoCalc (www.thermocalc.com), as a function of nickel content as shown in Fig. 1b. A nickel content of 6.5 wt.% gives the optimal austenite stability for transformation toughening at a yield strength of 160 ksi. An equilibrium ThermoCalc simulation (shown in Fig. 1b) predicts that tempering precipitates an austenite phase fraction of 0.11. Furthermore, the precipitated austenite phase is highly stable with enriched nickel content of 30% to deliver a substantial toughness enhancement. The presence of precipitated austenite with enriched nickel content has been verified with atom probe tomography as shown in Fig. 1a. The property objectives of BA-160 were validated experimentally by means of microhardness and Charpy impact tests. The results are summarized in Fig. 1d. A two-step heat treatment (30 min at 550 °C and 5 h at 450 °C) delivers the best combination of strength and toughness as indicated by the arrow in Fig. 1d.
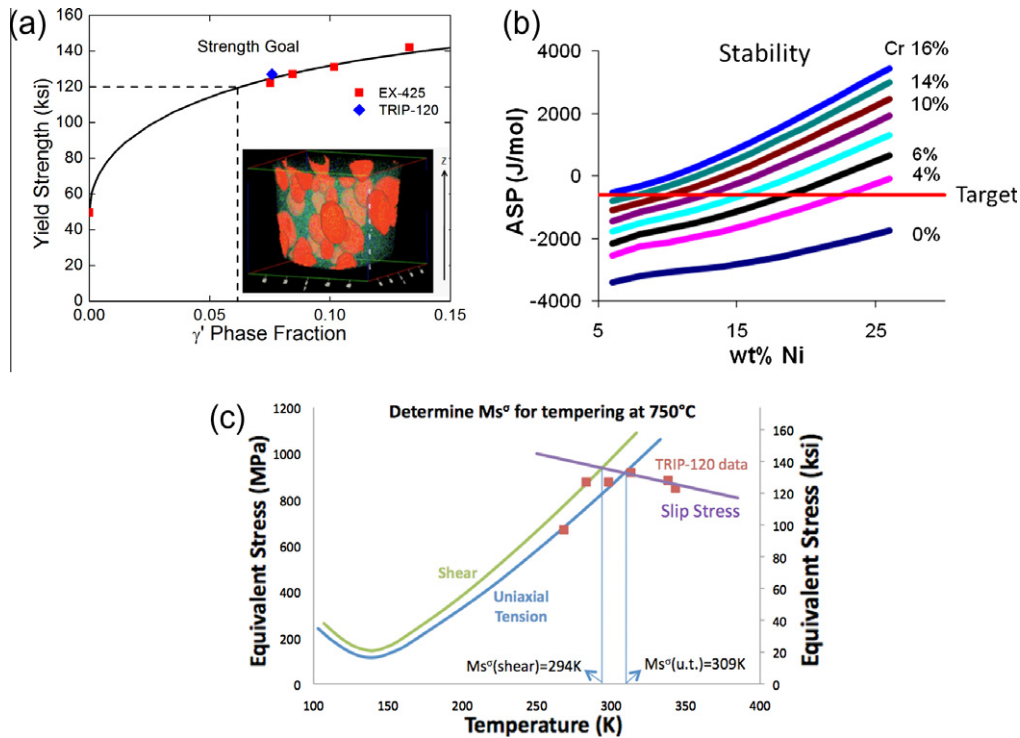
2.3. TRIP-120

While the blastalloy 160 martensite steel was designed to combine strength and toughness, FSI simulations of blast panel performance in an interdisciplinary design class project (Mckenna et al., 2007) demonstrated that further increases in blast protection could be achieved by optimizing steel designs to combine strength and uniform ductility (McCarren et al., March 2004). The TRIP-120 alloy was designed at Northwestern University in the doctoral research of Sadhukhan (2008) to achieve high strength (120 ksi) and sufficient toughness ($K_{Ic} \geqslant 90$ ksi/in$^{0.5}$) to avoid shattering, while

focusing on maximizing uniform ductility at room temperature. Additionally, there was a focus to achieve the proper austenite stability for shear instability resistance to improve its ballistic penetration resistance performance. In this design, transformation plasticity is used to delay shear instability driven by microvoid softening.

In order to achieve the strength goal of 120 ksi, the alloy is precipitation strengthened by the metastable $Ni_3(Al,Ti)$ γ' phase. The $Ni_3(Al,Ti)$ γ' phase has an L12 crystal structure, is coherent with the austenite matrix, and impedes dislocation shearing through anti-phase boundary formation (Asgari, 2001). The strengthening contribution that the γ' phase provides at an optimized particle size is defined quantitatively by the Ham model, which is shown graphically in Fig. 2a. This calibrated Ham model shows that a phase fraction of 0.063 corresponds to a yield strength of 120 ksi and determines the Al and Ti content in TRIP-120 and a temper at 750 °C for 10 h.

The primary objective in the design of TRIP-120 focuses on maximizing uniform ductility by making use of the transformation induced plasticity effect. The austenitic matrix must be designed with the proper transformation stability to stabilize plastic flow in order to maximize the uniform elongation. The stability of the austenitic matrix is defined by the M_s^σ temperature, which is the maximum temperature at which an elastic stress causes a martensitic transformation and is also stress-state dependent (see Fig. 2c). Hence, the M_s^σ temperature must be controlled to optimize TRIP-120 for uniform ductility. It is observed experimentally that uniform ductility under isothermal loading conditions is

Fig. 2. The design of TRIP-120 incorporates γ' precipitates to achieve the strength goal and controls the matrix composition to achieve the optimum stability for maximum uniform ductility at room temperature. (a) A calibrated Ham model predicts the yield strength as a function of the γ' phase fraction. Experimental data for EX-425 (Stavehaug, 1990) and TRIP-120 are plotted as square and diamond symbols. The size and number density of precipitates has been determined using the Local Electrode Atom Probe (LEAP), see inset; (b) a plot of the Austenite Stability Parameter (ASP) as a function of the Ni weight percent for various Cr contents are shown. The target ASP value has been calculated to design the M_s^σ temperature at -5 °C for optimal uniform ductility performance at room temperature and is shown in red; (c) A plot of the equivalent stress versus temperature shows the M_s^σ temperature under shear and uniaxial tension stress states. Experimental data points of TRIP-120 are shown in red. (For interpretation of the references to colour in this figure legend, the reader is referred to the web version of this article.)

maximized at temperatures $\sim$25 °C above M_s^σ in the uniaxial tension (ut) stress state (Leal, 1984), or the M_s^σ (ut). The M_s^σ (ut) for TRIP-120 is thus set to 5 °C to optimize the uniform ductility performance at room temperature. Combinations of Ni and Cr content were balanced until the critical austenite stability parameter (ASP) was met to deliver the desired M_s^σ (ut) temperature (Fig. 2b).

In this study, a 200 mm diameter ingot of TRIP-120 was produced by Smart Metals Corporation at New Hartford West Virginia by a vacuum induction melting technique, followed by vacuum arc remelting. The ingots were then shipped to Special Metals Corporation at Huntington West Virginia to be coated with anti-oxide barrier paint and homogenized at 1190 °C for 24 h. Break down forging was conducted at temperatures below 1093 °C. Upon completion of forging, the material was air cooled to room temperature. Finally, thin rolled plates of 6.5 mm thickness were obtained for machining of fluid–structure interaction samples.

The chemical composition of the three alloys is listed in Table 1.

3. Experimental approach

3.1. Fluid–structure interaction experiment

In this work, the experimental approach aims at reproducing, in a lab setting, underwater explosive loads as described in Cole (1948). During these events, a pressure wave is known to rise extremely fast to a peak pressure p_0 and then decay in an exponential fashion with a characteristic time t_0. Both p_0 and t_0 depend on the standoff distance from the explosion site. The total impulse is $p_0 t_0$.

In order to simulate such pressure loading in the laboratory, a scaled down fluid–structure interaction (FSI) experimental setup was developed by Espinosa et al. (2006). In the FSI experimental

Table 1
Chemical composition of HSLA-100, BA-160 and TRIP-120 in weight percent.

	HSLA-100	BA-160	TRIP-120
Cr	0.55	1.89	3.98
Ni	3.55	6.5	23.5
Mo	0.59	0.61	1.24
Ti	–	0.01	3.03
V	–	–	0.32
Al	0.03	–	0.16
C	0.04	0.05	0.01
Mn	0.84	0.001	–
B	–	–	0.012
N	128 ppm	–	10 ppm
Si	0.26	0.015	–
Cu	1.58	3.33	–
Nb	0.029	–	–
Fe	Balance	Balance	Balance

setup, the shell of a naval hull is scaled down to a panel clamped at one end of a shock tube filled with water. A water piston seals the other extremity of the chamber and the exponentially-decaying pressure history is produced by impacting the water piston with a flyer plate (Espinosa et al., 2006). After impact, pressure waves propagate through the water column and reach the panel. The circular part of the panel in contact with water (152.4 mm in diameter) is subjected to the pressure wave. The experimental setup is schematically shown in Fig. 3. The tested panel is characterized by its radius L, thickness h, density ρ and dynamic yield stress σ_y^d. When the panel deforms, water cavitation is elicited inside the chamber. The fluid–structure interaction results in panel deflection, which is characterized experimentally by means of shadow Moiré and high speed photography using a Cordin 220-8 high
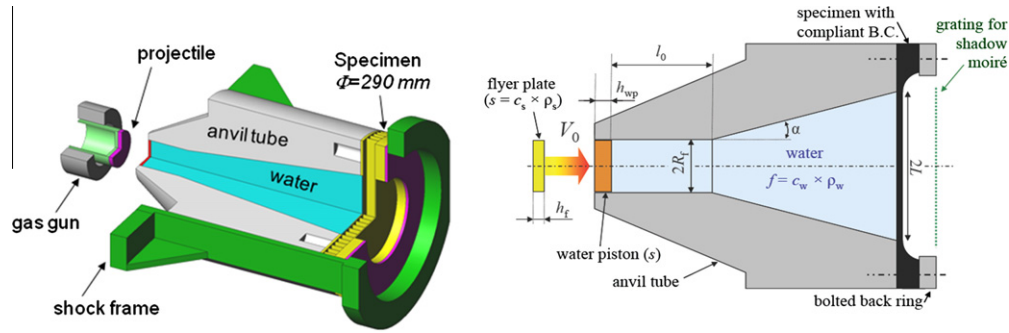
Fig. 3. Experimental setup to simulate impulsive underwater pressure loadings of structures.

speed intensified CCD camera. The reader interested in the details of this experimental setup will find a complete description in Espinosa et al. (2006). In earlier investigations, this setup was used to assess the performance of hard core steel sandwiches (pyramidal truss core, square honeycomb) (Mori et al., 2007) and soft core sandwich panels in terms of blast mitigation and momentum transfer capabilities (Mori et al., 2009).

The pressure wave created by the impact of the flyer plate on the water piston is a function of flyer initial velocity V_0, material impedance and flyer plate/water piston dimensions. We found from FEA simulations that the generated impulse is also sensitive to other features, such as the geometry of the anvil tube, dimensions and plastic flow of projectile and water piston. This becomes significant at the impact velocities needed to fail the high strength steel alloy panels here investigated. Therefore, in this regime, the one-dimensional analytical solution introduced in (Espinosa et al., 2006) was not employed to estimate the applied impulses. Separate simulations were performed on water columns extending beyond the location where the tested panel was placed. By keeping other experimental conditions identical (such as flyer plate velocity, geometries of anvil, flyer plate, and water piston), the applied impulse for each experiment was obtained by numerically integrating the pressure history at the location of the tested panels.

3.2. Specimen geometry

Prior work showed that transverse shear failure at the clamping region can become a dominant failure mode in uniform thickness panels subjected to impulsive loading. Such failure mode prevents necking and fracture in the center of the panel (Nurick and Shave, 1996), which is more representative of failure in naval structures. Hence, in this work the specimens were designed to limit shear stress concentrations at the boundary by adding compliance at the edges of the pressurized region. In doing so, biaxial stretching in the center of the panel becomes dominant and thus representative of the stress state leading to failure in marine structures. For similar reasons, this type of compliant boundary condition was already introduced for sandwich structures (Mori et al., 2009). Here, the compliance is obtained by tapered round flanges between the gage part and the ring part of the sample as shown in Figs. 4 and 5. The samples were machined from hot rolled plates of two different thicknesses. Hence, two different sample dimensions were employed, see Figs. 4 and 5.

4. Modeling approach

4.1. Constitutive model description

In this investigation, the extended Gurson model developed by Hutchinson and co-workers (Nahshon and Hutchinson, 2008; Xue
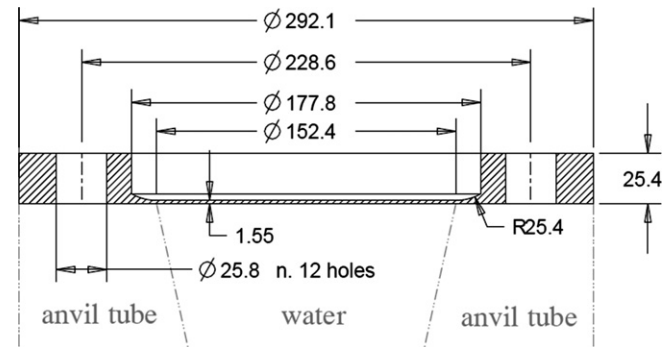

Fig. 4. Cross section drawing of the 25.4 mm thick sample. The anvil tube and water column contours are plotted in phantom lines. Dimensions are in mm.
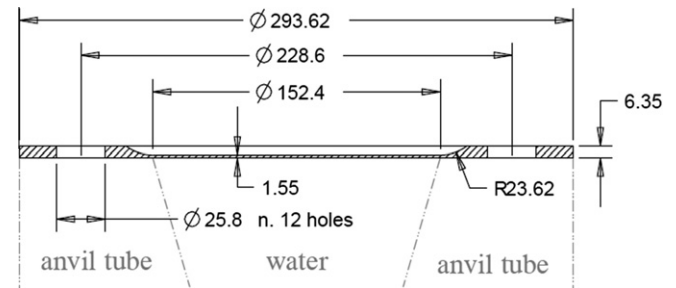

Fig. 5. Cross section drawing of the 6.35 mm thick sample. The anvil tube and water column contours are plotted in phantom lines. Dimensions are in mm.

et al., 2010) is used. This model is an augmentation of the original Gurson model, which was formulated in mean stress-effective stress space to describe flow and rupture of ductile materials due to void growth (Gurson, 1977). In order to capture void growth under more complex loading conditions, the extended Gurson model (Nahshon and Hutchinson, 2008) includes the effect of the third stress invariant in the evolution equation for void volume fraction. The yield surface is given in terms of effective stress, σ_e, and mean stress, σ_m, namely,

$$F(\sigma_e, \sigma_m, f) = \left(\frac{\sigma_e}{\sigma_M}\right)^2 + 2f^* q_1 \cosh\left(\frac{3q_2\sigma_m}{2\sigma_M}\right) - (1 + q_3 f^{*2}) \qquad (1)$$

where σ_M is the current effective flow stress of the damage-free matrix material, f is the current void volume fraction, and $q_1 = 1.5$, $q_2 = 1$ and $q_3 = 2.25$ are fitting parameters introduced by Tvergaard (1990), which mainly impact the triaxiality sensitivity of the model but also the interaction between plastic yield and damage. To capture more accurately the loss of stress carrying capacity, f^* in Eq. (1)

is a piecewise function introduced in Tvergaard (1990) following a growth-coalescence concept and states

$$f^*(f) = \begin{cases} f, & f \leqslant f_c \\ f_c + \frac{1/q_1 - f_c}{f_f - f_c}(f - f_c) & f_c < f \leqslant f_f \end{cases} \quad (2)$$

where f_c is the critical value of the void volume fraction indicating the onset of coalescence and f_f is the value of the void volume fraction at failure. In this study, f_c and f_f are 0.15 and 0.25, respectively, which correspond to the values used in (Xue et al., 2010).

The evolution of the void volume fraction is given by

$$\dot{f} = (1-f)D^p_{kk} + k_\omega f \omega(\boldsymbol{\sigma}) \frac{s_{ij}D^p_{ij}}{\sigma_e} \quad (3)$$

where s_{ij} is the stress deviator, D^p_{ij} is the plastic strain rate, k_ω is called the shear damage coefficient, and $\omega(\boldsymbol{\sigma})$ is a non-dimensional measure given by

$$\omega(\boldsymbol{\sigma}) = 1 - \left(\frac{27J_3}{2\sigma_e^3}\right)^2 \quad (4)$$

in which $J_3 = \det(\mathbf{s}) = \frac{1}{3}s_{ij}s_{ik}s_{jk}$ is the third stress invariant.

4.2. Model calibration

The extended Gurson model was calibrated by simulating dynamic tension and shear experiments performed on the HSLA-100, BA-160 and TRIP-120 steel alloys at high strain rate ($\sim 10^3 \, s^{-1}$). A stored-energy Kolsky bar apparatus was used. The tension and shear loading pulses are generated by the sudden release of elastic energy stored in the incident bar. The energy is produced by hydraulic double acting actuators. Signals on the strain gages on the incident and transmitted bars were recorded and processed to obtain the stress, strain and strain rate evolutions assuming the sample is in equilibrium. The maximum strain rate can reach up to $2 \times 10^3 \, s^{-1}$. Experiment details can be found in the previous report (Latourte et al., 2010). As suggested by the FSI finite element modeling discussed in the following section, the strain rate experienced by the steel panels is on the order of $10^3 \, s^{-1}$. Therefore, $10^3 \, s^{-1}$ was chosen as the reference strain rate for evaluating the dynamic responses of steels in this study. Two key parameters for each steel were identified based on the tensile and shear experimental data: the initial void volume fraction, f_0, and the shear damage coefficient, k_ω. A true stress–strain curve of the form $\sigma_T = \sigma_T^{neck}(\varepsilon_T/\varepsilon_T^{neck})^N$ was assumed beyond the necking point, where σ_T^{neck} and ε_T^{neck} are the true stress and strain at necking. The hardening exponent N is taken as ε_T^{neck}. Since k_ω has little effect on the dynamic tensile experiments (Nahshon and Hutchinson, 2008), the initial void volume fraction f_0 was identified first based solely on the nominal stress–strain response obtained from dynamic tensile experiments. The parameter f_0 was then kept constant and the other coefficient k_ω was identified based on the nominal shear stress-shear strain response obtained from thin-walled dynamic shear experiments. In this study, both parameters f_0 and k_ω were identified for HSLA-100 and TRIP-120, and for BA-160 we only identified f_0 from dynamic tensile experiments, while k_ω was assumed to be the same as that for HSLA-100. This assumption is based on the fact that these two martensitic steels exhibit a very similar inelastic behavior up to failure, with the main difference being their strength. Furthermore, this assumption is supported by the observation of similar martensitic microstructure in the two materials. While shear failure could play a role in the clamping boundaries of the steel panel, the experimentally observed failure occurs at the center of the panel where the material undergoes biaxial stretching. Therefore, in FSI experiments void growth under tension appears to be the dominant failure mechanism. The calibrated f_0 and k_ω for each steel are listed in Table 2.

Table 2
Calibrated extended Gurson model coefficients for different steels.

Alloy	σ_T^{neck} (MPa)	N	f_0	k_ω
HSLA-100	941	0.04	4×10^{-4}	12
BA-160	1372	0.07	1.2×10^{-3}	12
TRIP-120	1332	0.12	0.075	3

The shear damage coefficient, $k_\omega = 12$, for HSLA-100 and BA-160 is higher than those typical for lower strength steels in quasi-static tension (Xue et al., 2010). This is probably due to the contribution of microvoid nucleation not accounted for in the extended Gurson model (Rittel et al., 2008, 2006). Therefore, the unusually high k_ω for HSLA-100 and BA-160 may result from both void nucleation and coalescence.

A comparison between the identified model and the experimental data is shown in Fig. 6a and b. The deformed sample geometries, as predicted by the model, are shown in Fig. 6c and d; for dynamic tension and shear, respectively. The constitutive description accurately captures the macroscopic strain softening and damage of alloys under dynamic tension. For HSLA-100, the true strain at failure, ε_T^{fail}, is about 120%, which compares well with the experimental value of 117% reported in (Xue et al., 2010). The post-yield hardening observed in the dynamic torsion data is not as well described by the model. Indeed, as shown in Fig. 6b, the HSLA-100 steel alloy exhibits an "extra" strengthening behavior compared with the shear behavior predicted by the extended Gurson model. This might be due to deformation mechanism, which had not been accounted for in the present model, such as roll-induced anisotropy and recrystallization. However, the calibrated model is able to capture the drop in shear strain, as a result of shear localization due to growth and coalescence of voids, which resulted in sample failure.

The dynamic tensile experimental results show a higher uniform ductility (i.e., strain at the onset of necking) in TRIP-120 than in HSLA-100 or BA-160. However, the HSLA-100 and BA-160 steel alloys exhibit excellent post-necking ductility. The TRIP-120 alloy shows higher strength, higher uniform ductility, and significantly more hardening rate than the reference martensitic alloy HSLA-100. The BA-160 alloy, exhibits a much higher strength than HSLA-100 and a very similar post-necking ductility.

Even though the calibrated extended Gurson model captured the dynamic tensile behavior of TRIP-120, the initial void volume fraction $f_0 = 0.075$ was too high to have a reasonable physical meaning. This suggested that the failure mechanism for TRIP-120 was not only void coalescence but also micro-cracks. As reported in (Latourte et al., 2010), plastic deformation mechanisms for TRIP-120 in the temper condition tested here were found to include void growth, martensitic transformation, and grain boundary fracture due to cellular precipitation reactions. Moreover, dynamic torsion tests on TRIP-120 had shown that shear strain hardening and failure mechanisms were highly dependent on the martensitic phase transformation in the material. Since the extended Gurson model does not account for phase transitions, it is not surprising that the torsion behavior of TRIP-120 predicted by the FEA model did not agree particularly well with the experimental data. For this reason and given that TRIP-120 exhibited damage involving both microcracking and void growth, numerical modeling of FSI experiments performed on TRIP-120 was not attempted.

4.3. FSI numerical model

Finite element analysis of the underwater impulsive loading experiments was conducted using the code Abaqus/Explicit v6.8-2. The extended Gurson model as presented in Section 4.1
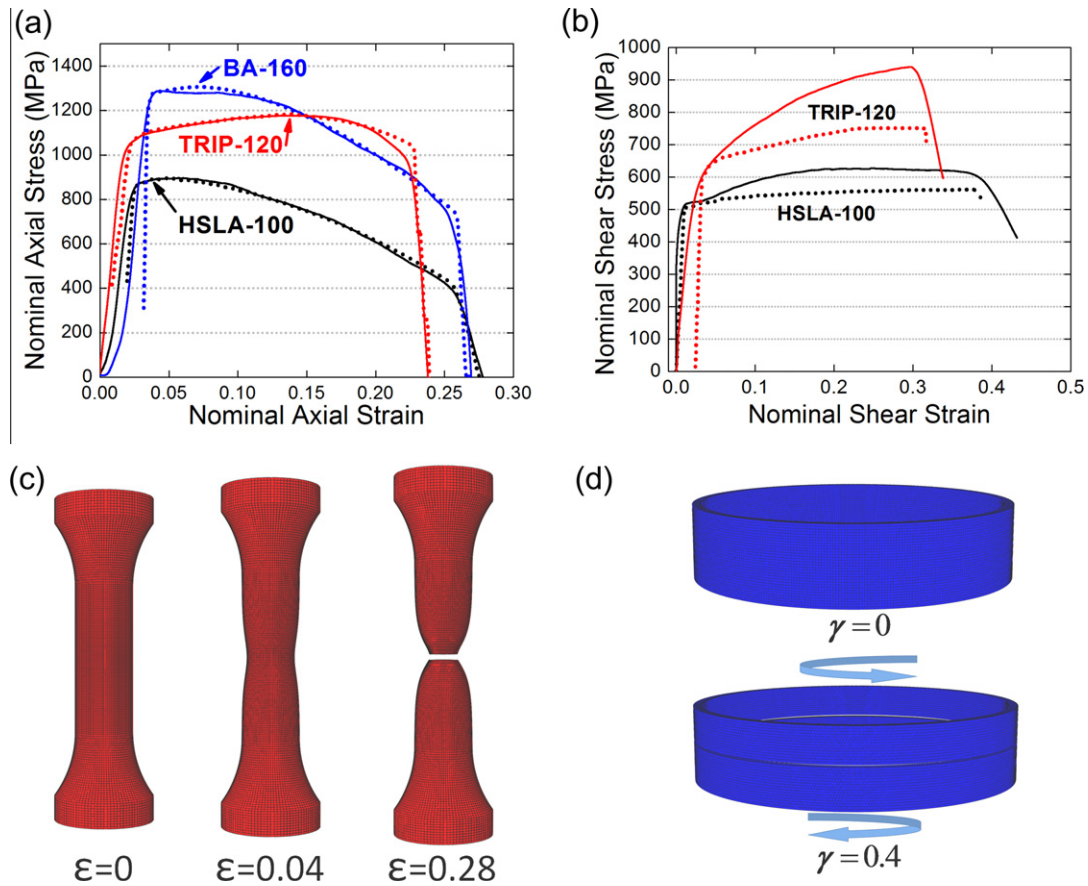
Fig. 6. Comparison of experimental data and extended Gurson model results for dynamic tensile and shear tests. (a) nominal axial stress vs. axial strain curves of dynamic tensile tests for three alloys (solid curves) compared with calibrated extended Gurson model simulation results (dashed curves). Arrows indicate onset of necking; (b) nominal shear stress vs. shear strain curves of dynamic shear tests for HSLA-100 and TRIP-120 (solid curves) compared with calibrated extended Gurson model simulation results (dashed curves). It is known that Kolsky bar experiments require wave reverberations in the sample before a homogeneous deformation at approximately constant strain rate develops in the sample. Hence, the start of the stress vs. strain responses predicted by numerical simulations was shifted to compare with corresponding experimental results; (c) FEA results for HSLA-100 dynamic tension failure as predicted by the extended Gurson model; (d) FEA deformation results for HSLA-100 dynamic torsion failure as predicted by the extended Gurson model.

was implemented using the user defined subroutine, VUMAT, adopted from (Xue et al., 2010). A three dimensional coupled Eulerian and Lagrangian (CEL) technique was used to simulate the fluid–structure interaction. We employed a coupled Eulerian–Lagrangian approach because when a Lagrangian formulation is employed for the water column, excessive mesh distortion occurs at the high impulses needed to fail the panels. Hence, in this investigation, the water column was modeled by 8-node linear brick elements with reduced integration. Eulerian elements of size $2.5 \times 2.5 \times 2.5$ mm^3 were used. The steel panel, anvil tube, projectile and water piston were modeled by Lagrangian 8-node linear brick elements with reduced integration. The steel panel was meshed with an in-plane element size of 0.6×0.6 mm^2 and 10 elements throughout the thickness. The anvil tube had a minimum element size of $3 \times 3 \times 3$ mm^3. The element sizes of projectile and water piston was chosen to be $1 \times 1 \times 1$ mm^3.

It is worth mentioning some differences with the experiments and simulations reported in (Espinosa et al., 2006), namely, the use of a ductile brass projectile in lieu of a hardened AISI 4140 steel projectile, and the modified design and clamping of the tested plate to avoid boundary shearing off failure. Brass was chosen to limit the damage that can potentially occur in the anvil tube at high impulses. The new brass projectile was of greater thickness (about 10.15 mm instead of 4.8 mm) to create the higher impulse needed to deform and fail the high strength materials here investigated.

An elasto-plastic constitutive response was used to model the flyer, piston and anvil. The coefficients of the constitutive behaviors used in the simulation are listed in Table 3.

5. Results

5.1. FSI experiments

A summary of performed experiments and associated experimental parameters are reported in Table 4, in which I_0 represents the free-field applied impulse. In addition, for each test a non-dimensional impulse $\hat{I} = I_0/(h\sqrt{\rho\sigma_y^d})$ is reported, in which h and ρ are the thickness and density, and σ_y^d is the dynamic yield stress (at a strain rate of $\sim 10^3$ s^{-1}). The non-dimensional impulse indicates how the response of a thin plate under impulsive loading scales with materials' density and strength. In all experiments, except for the one on BA-160, a water piston thickness $h_{wp} = 10.6$ mm was used. The piston material used in each experiment was the same as the one used for the flyer plate. Flyer plates with thickness h_f <5 mm were machined from 4340 steel. Flyer plates with thickness h_f >10 mm were machined from brass. All specimens had the same thickness of approximately 1.55 mm, which gave a consistent areal mass $\bar{M}$ of about 12.2 kg/m^2 taking the density of the alloys ρ equal to 7870 kg/m^3.

Table 3
Constitutive model coefficients used in the FEA for the materials of the experimental setup.

Material properties	Symbol	Units	Brass	Wrought 4340 steel	Water
Young's Modulus	E	GPa	105	205	–
Poisson's ratio	v	–	0.35	0.29	–
Density	ρ	kg/m^3	8750	7850	998
Yield stress	σ_y	MPa	427	470	–
Mie–Grüneisen equation of state for water					
Sound velocity	c_f	m/s	–	–	1490
EOS coefficient	s_1	–	–	–	1.92
Grüneisen coefficient	Γ_0	–	–	–	0.1
Dynamic viscosity	μ	Pa s	–	–	1×10^{-3}

Table 4
List of experiments conducted on monolithic panels at low and high impulses.

Material Exp. #	V_0 (m/s)	h_f (mm)	h_{wp} (mm)	σ_y^d (MPa)	I_0 (Pa s)	$\hat{I} = I_0/(h\sqrt{\rho\sigma_y^d})$	$(\frac{\delta}{L})_{max}$	Fracture (yes/no)
HSLA-100								
1	289	10.18	10.6	810	4279	1.09	0.367	No
2	328	10.18	10.6	810	5080	1.30	0.420	No
TRIP-120								
1	322	4.84	10.6	995	1042	0.24	0.119	No
2	325	10.16	10.6	995	4854	1.12	0.361[a]	Yes
3	364	10.16	10.6	995	5674	1.31	0.418[a]	Yes
BA-160								
1	350	14.94	14.93	1234	7108	1.47	0.497	No

[a] The non-dimensional peak deflection was obtained prior to fracture.

5.1.1. HSLA-100

Two HSLA-100 samples were machined from 1″ thick rolled plates. The plates were heat treated before being machined, following the heat treatment recipe described in Section 2.1. Sample 1 was tested at a non-dimensional impulses of $\hat{I} = 1.09$ and sample 2 was tested at $\hat{I} = 1.30$ (see Table 4).

Shadow Moiré images were recorded by means of high speed photography and used to compute deflection profiles following the procedure detailed in Espinosa et al. (2006). Deflection profiles were computed along the specimen center. These profiles are plotted in Fig. 7a and compared with deflection profiles obtained from FEM simulations based on the extended Gurson model described in Section 4.1, see Fig. 7b. A deformation profile was also measured along the sample diameter, after the experiment, using a marble and gage indicator. This profile is reported as "final profile" and is plotted in black dashed line in Fig. 7a. Comparison of Fig. 7a and b, reveals that experimental and simulated profiles correlate very well, at various instances in time, and that center deflections are also in very good agreement. The maximum center deflection

predicted by the FEA was about 27.5 mm while the experimental one was 27.9 mm. Likewise, the limited spring back was well captured by the FEM simulation. The FEA results for HSLA-100 sample 2, $\hat{I} = 1.3$, also show excellent agreement with the experimental measurements. The maximum deflection from the FEA was 32.6 mm while the experimental measurement was 32.0 mm.

A plasticity study was conducted for the HSLA-100 sample 2 tested at $\hat{I} = 1.30$. After the experiment, the panel was sliced along a diameter with a water jet. The thickness along the diameter, 5 mm from the cut, was measured using a micrometer. These measurements were used to compute the thickness reduction with respect to the initial thickness h_0 of 1.55 mm. The thickness reduction profile obtained from numerical simulation is plotted and compared to experimental measurements in Fig. 8. A sharp thickness reduction in the center region of the panel (about 2 mm in diameter) suggests the occurrence of necking. FEA results give an equivalent strain at the center of the panel, $\varepsilon^{eq} = 24.3\%$. According to (Hutchinson and Neale, 1978), the necking strain in equibiaxial tension is larger than that in plane-strain tension but
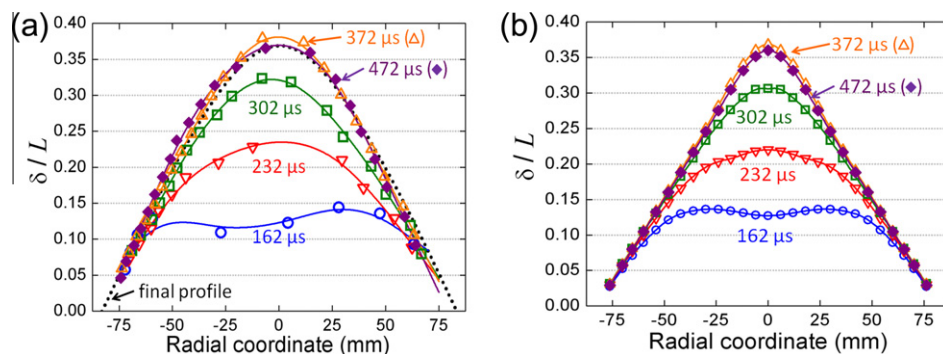
Fig. 7. Deflection profile evolution of HSLA-100 sample 1 tested at $\hat{I} = 1.09$, (a) deflections obtained from shadow Moiré and postmortem measurement (final profile), (b) deflections obtained from FEA.
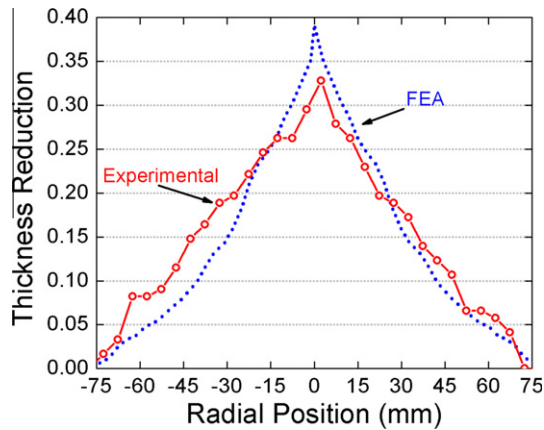
Fig. 8. Comparison between experimental (red circle) and numerical simulation (dash line) results of thickness reduction profile of HSLA-100 sample 2 tested at $\hat{I}$ = 1.3. (For interpretation of the references to colour in this figure legend, the reader is referred to the web version of this article.)

equal or less than that in uniaxial tension. Therefore, ε^{eq} given by the FEA results lies in between the necking strain and the failure strain of HSLA-100 (Section 4.2), which is consistent with the absence of fracture in the tested specimen.

5.1.2. TRIP-120

Three panels of TRIP-120 material were machined from 6.35 mm plates following the design presented in Fig. 5. Samples 1 and 2 were solutionized before machining, and then tempered for 10 h followed by a nitrogen quench. Sample 3 was solutionized and clamp tempered before machining to ensure a good flatness of the plate. Non-dimensional impulses $\hat{I}$ of 0.24, 1.12 and 1.31 were applied. The impulse of $\hat{I}$ = 0.24 is referred to as "low impulse", while the two others are referred as "high impulses". Shadow Moiré images were recorded for samples 1 and 3.

For the TRIP-120 panel tested at a normalized impulse $\hat{I}$ = 0.24, the grating pitch was 1 mm and it was placed at a distance of 27 mm from the sample air side. The low deflection combined with the high grating pitch did not enable the computation of deflection profiles from the shadow Moiré technique. However, the final deformed profile was measured on the water side surface of the sample. The water side was chosen because it allows the measurement of deflections even within the tapered region, and, hence, to assess the boundary condition compliance. The final center deflection of this sample was 9.1 mm (corresponding to δ/L = 0.119).

Two TRIP-120 samples were tested at normalized impulses of $\hat{I}$ = 1.12 (sample 2) and $\hat{I}$ = 1.31 (sample 3). Sample 2 exhibited a fracture pattern consistent with biaxial tension, Fig. 9b. Fracture initiated at the panel center and propagated circumferentially followed by petaling. Fracture surface analysis provided insight on the TRIP-120 fracture behavior under biaxial stretching conditions. A field emission scanning electron microscope (SEM) was used to image the fracture surface of the sample, Fig. 9b and c. The images suggest a shear fracture mode. Elongated dimples are observed at high magnification, Fig. 9c. SEM images taken on the surface of the sample (air side) show dense arrays of micrcracks at a scale finer than the average grain size of 30 μm, see Fig. 9d. This surface microcracking shows a circumferential preferential orientation (the radial direction is indicated by vector $\vec{r}$ in Fig. 9d), along which stretching is maximal. As observed in the fractography reported in (Latourte et al., 2010), the TRIP-120 alloy exhibits a combination of ductile (voids) and brittle (microcracking) damage.

TRIP-120 sample 3 was tested at an impulse $\hat{I}$=1.31 and fracture was also observed. High speed camera pictures were recorded during the experiment, see Fig. 10. The pictures show an increasing

number of concentric fringes up to t = 240 μs. The apex, which corresponds approximately with the center of the fringes, is at the panel center. At t = 310 μs, a distortion of the fringes can be observed in the bottom part of the panel, and on the subsequent pictures a second bulge appears at that location. At t = 450 μs, a vertical crack appears across the localized bulge. On the final picture at t = 550 μs, the crack has propagated across the whole pressurized region of the specimen.

The deformation evolution for TRIP-120 sample 3 is plotted in Fig. 11. The experimental points are obtained every half fringe variation and are plotted with colored symbols. These points were used to compute approximation splines that are plotted in solid lines of the same color. From the plots, one can notice that when the second bulge starts at t = 310 μs, the deflection is not symmetric with respect to the radial coordinate. Moreover, from the deflection profile at t = 450 μs, the peak deflection before fracture is inferred to be 31.9 mm (δ/L = 0.418).

SEM microscopy was conducted on an area of the fracture surface close to the identified fracture initiation point. A mixture of ductile (void sheets) and microcracks are observed, Fig. 12a. A magnified view of region C* shown in Fig. 12b, reveals intergranular fracture, which was associated to a grain boundary cellular reaction in (Latourte et al., 2010).

5.1.3. BA-160

A BA-160 panel was machined from 6.35 mm plates following the design presented in Fig. 5. The dynamic material characterization tests have shown that BA-160 distinguishes itself from the three examined steels by having the highest yield strength and excellent post-necking ductility. To load the BA-160 panel as close as possible to the onset of failure, a very high impulse is required. Due to restrictions in the kinetic energy the overall FSI set up can withstand, a maximum flyer velocity of 350 m/s was employed. Hence, to maximize the free-field impulse while retaining a significant FSI effect, the thickness of the brass water piston and flyer was set to 14.94 mm and 14.93 mm, respectively. The resulting free-field impulse was computed to be 7108 Pa s, which corresponds to a non-dimensional impulse $\hat{I}$ = 1.47. Under these conditions, no catastrophic failure was observed in the tested BA-160 panel. Furthermore, no appreciable microvoid or microcrack was found on the specimen, indicating the sample still retained the capability to sustain even larger blast loading. Analyses of the shadow Moiré images yielded a peak central deflection of 37.9 mm, corresponding to a normalized maximum central deflection of δ/L = 0.497.

5.2. Performance predictions from the extended Gurson model

Based on the good correlation observed between FEA and FSI experimental results for the HSLA-100 alloy panels, Section 5.1.1, estimation of panel performance up to failure due to necking instability and fracture was pursued. The analysis is based on the material model predictive capabilities established for the extended Gurson model, based on the parametric identification reported in Section 4.2. Moreover, by combining the extended Gurson model and the coupled Eulerian–Lagrangian finite element analysis, two key elements in the analysis of structures subjected to underwater impulsive loads are accurately modeled: (i) the fluid–structure interaction leading to water cavitation, and (ii) damage and failure of the panels as a result of void growth and coalescence. In the performed numerical simulations, thickness of projectile and water piston, and the initial projectile velocity were increased until impulses leading to failure were identified. It is also worth mentioning that all the experiments in this study have significant FSI effect. According to Xue and Hutchinson (2004), the time scale characterizing the fluid–plate interaction is $t_* = (\rho h)/(\rho_f c_f)$, where
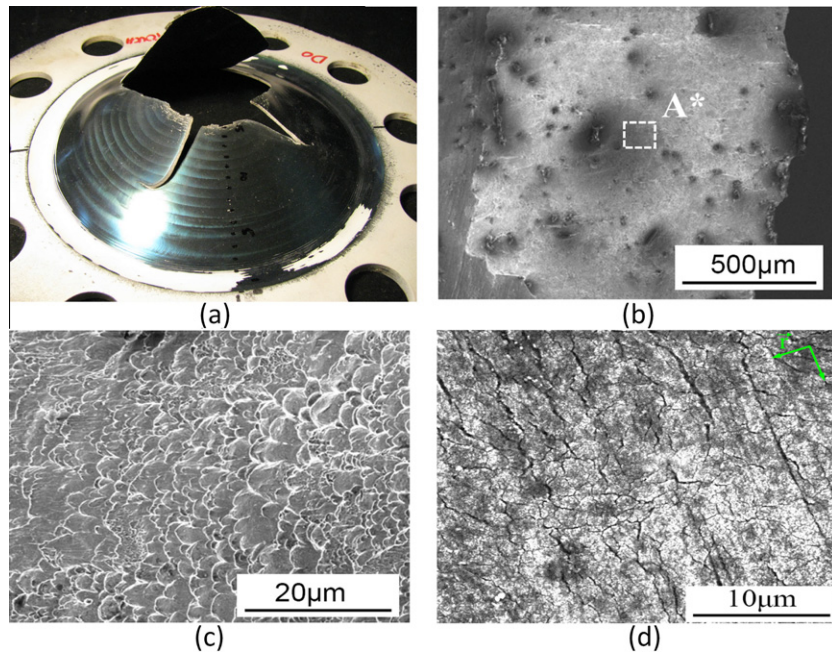
Fig. 9. (a) TRIP-120 sample 2 after fracture; (b) SEM micrograph of fracture surface of TRIP-120 sample2; (c) highlight of area A* in subplot (b); (d) microcrack on air side of sample due to tensile stretching. Cylindrical coordinate is shown in upper right corner of subplot (d) with $\vec{r}$ being the radial vector.
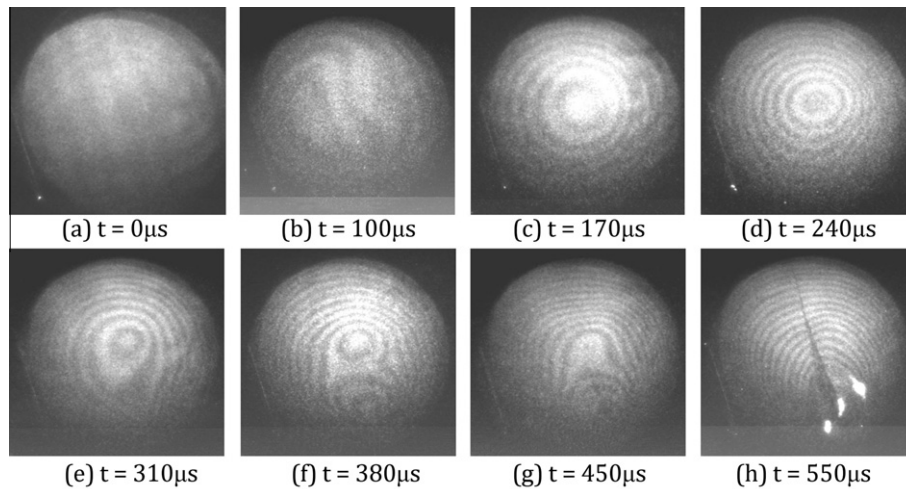
Fig. 10. Evolution of shadow moiré for TRIP-120 sample 3 during FSI test. $t = 0$ μs corresponds to time when blast wave reaching sample.

ρ and h are the density and thickness of the plate; ρ_f and c_f are the density of the fluid and sound speed in the fluid. In this study, $t_* \sim 8.2$ μs. The decay time of the free-field impulse is $t_0 \sim 57.6$ μs, as determined from the FEM analysis. In other words, all the experiments in this study approach the limit where $t_0/t_* \gg 1$. The ratio of the impulse imparted to the plate to the free-field impulse, I/I_0, can be approximated by $2(t_0/t_*)^{t_0/(t_*-t_0)} \sim 0.21$. This strong FSI effect was well captured by the coupled Eulerian–Lagrangian formulation. Fig. 13 shows the FEA results for the failure of a HSLA-100 steel panel under the non-dimensional impulse, $\hat{I} = 1.89$. Water cavitation at the panel center develops at about 0.25 ms after panel impulsive loading (Fig. 13a). The cavitation region then disappears followed by a severe plastic deformation of the panel, which leads to material failure. As shown in Fig. 13b, the FEA with the extended Gurson model predicts a cross-shaped failure pattern, which is consistent with experimental observations of petaling.

Table 5 lists configurations and results for HSLA-100 and BA-160 alloys. Fig. 14a summarized the impulse per areal mass vs. normalized center deflection responses for the three alloys both from experiments and numerical simulations. The predicted performance of the BA-160 steel panels agrees very well with the experimental result, indicating the Gurson model successfully predicts the response of the BA-160 steel under dynamic loadings conditions. Furthermore, the study reveals that BA-160 panels can sustain the highest impulse prior to failure. It also exhibits the best performance, i.e., lowest central deflection for a given impulse per unit areal mass. The improvement in performance with respect to HSLA-100 panels is the result of the alloy higher dynamic yield strength and similar uniform ductility and post-necking ductility. For each alloy, a slight deviation from the original linear impulse-deflection relationship is observed in the high range of impulses preceding failure, which corresponds to the onset of extensive void growth and coalescence in the material. Both,
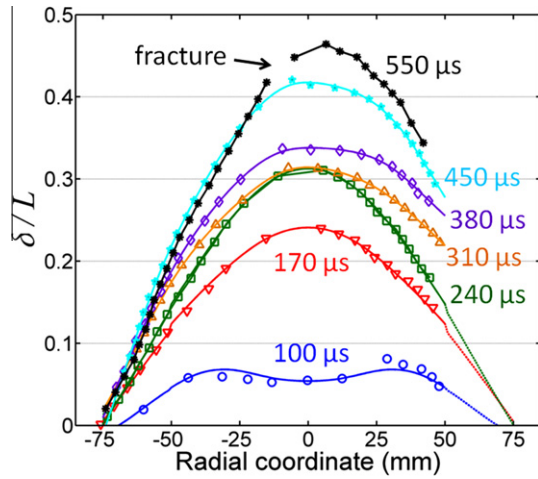
Fig. 11. Deflection profile evolution of TRIP-120 sample 3 tested at $\hat{I}$ = 1.31 obtained from shadow moiré.

HSLA-100 and BA-160 alloys could sustain a certain increase of impulse, beyond the linear regime, without failure probably because of their excellent post-necking ductility as discussed in Section 2.

FSI experiments on clamped circular panels of different materials such as steel, titanium (Symonds and Wierzbicki, 1979), mild steel (Nurick and Martin, 1989a,b), HSLA steel (Rajendran and Narashimhan, 2001), 6061-T6 aluminum, 1018 steel (Florence, 1966), and 5010 steel (Ashani and Ghamsari, 2007) have been interpreted in normalized impulse-normalized center deflection. Such interpretation is based on the analysis performed by Jones (1989), who introduced finite displacement enrichment to the analysis of rigid-plastic deformation of clamped plates. The result is:

$$\frac{\delta}{h} = \frac{1}{2}\left(\left(1 + \frac{2}{3}\lambda\right)^{\frac{1}{2}} - 1\right) \text{ with } \lambda = \frac{4I_0^2 L^2}{\bar{M}\sigma_y h^3} \qquad (5)$$

in which δ is the maximum center deflection, h and L are the panel thickness and radius, respectively. The prediction given by Eq. (5) is often presented as a reference solution in several experimental studies (Ashani and Ghamsari, 2007; Florence, 1966; Rajendran and Narashimhan, 2001), in which the yield stress σ_y is either static yield stress σ_y^s or dynamic yield stress σ_y^d. The latter case is often referred as to the modified Jones equation. Here, a simplified linear relationship (Symonds and Wierzbicki, 1979; Teeling-Smith and Nurick, 1991) is adopted to describe the performance of clamped circular panels in FSI experiments, namely,

$$\frac{\delta}{L} = \alpha\hat{I} + \beta \qquad (6)$$

in which α and β are constants, and $\hat{I}$ is the non-dimensional impulse given by

$$\hat{I} = \frac{I_0}{\bar{M}}\sqrt{\frac{\rho}{\sigma_y^d}} = \frac{I_0}{h\sqrt{\rho\sigma_y^d}}. \qquad (7)$$

When the dynamic yield stresses for HSLA-100, TRIP-120 and BA-160 (810 MPa, 995 MPa and 1.234 GPa, respectively) are employed the linear fitting given by Eq. (7) yields: $\alpha = 0.3282$ and $\beta = -7 \times 10^{-4} \sim 0$. Fig. 14b shows the scaled non-dimensional impulses vs. normalized center deflections, as given by Eq. (6), in which a universal response is obtained.
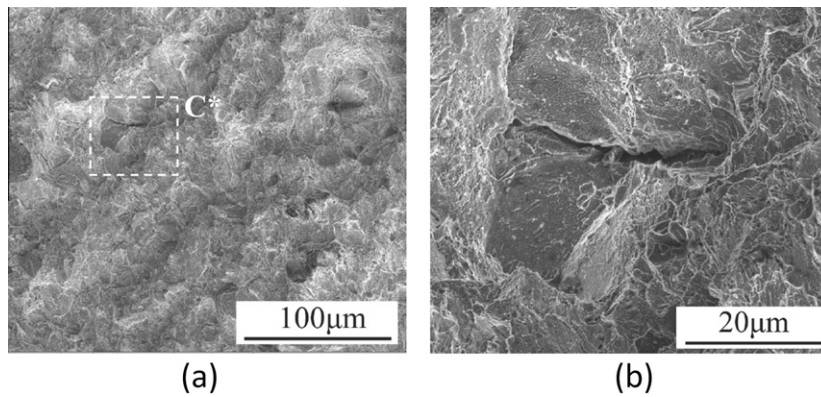

Fig. 12. (a) SEM micrographs of fracture surface of TRIP-120 sample 3 tested at $\hat{I}$ = 1.31 around strain localization point; (b) magnified view of area C* in subplot (a).
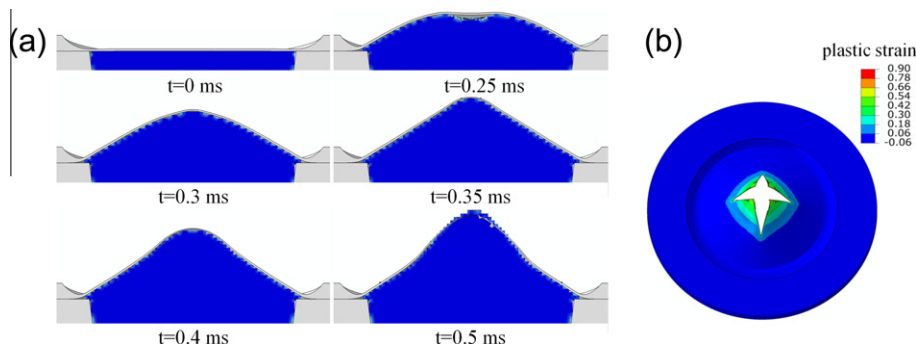

Fig. 13. FEA results for HSLA-100 steel panel subjected to a normalized impulse $\hat{I}$ = 1.89. (a) Evolution of HSLA-100 steel panel deformation (t = 0 corresponds to the time when blast wave reaches the sample); (b) failure pattern for HSLA-100 steel panel as predicted by the extended Gurson model.

Table 5
List of FEA simulations for HSLA-100 and BA-160 alloys.

Exp. #	V_0 (m/s)	h_{wp} (mm)	h_f (mm)	I_0 (Pa s)	$\hat{I}$	$\left(\frac{\delta}{L}\right)_{max}$	Fracture (yes/no)
HSLA-100							
2	328	10.6	10.18	5080	1.3	0.428	No
3	330	12	12	5966	1.52	0.505	No
4	330	14	14	6667	1.7	0.564	No
5	360	14	14	7190	1.84	0.654	No
6	370	14	14	7407	1.89	0.682[a]	Yes
BA-160							
1	289	10.6	10.18	4279	0.89	0.291	No
2	328	10.6	10.18	5080	1.05	0.345	No
3	330	12	12	5966	1.24	0.402	No
4	330	14	14	6667	1.38	0.445	No
5	370	14	14	7407	1.53	0.496	No
6	390	14	14	8141	1.69	0.549	No
7	420	14	14	8872	1.84	0.601	No
8	430	14	14	9150	1.89	0.630[a]	Yes

[a] The non-dimensional peak deflection was obtained prior to fracture.
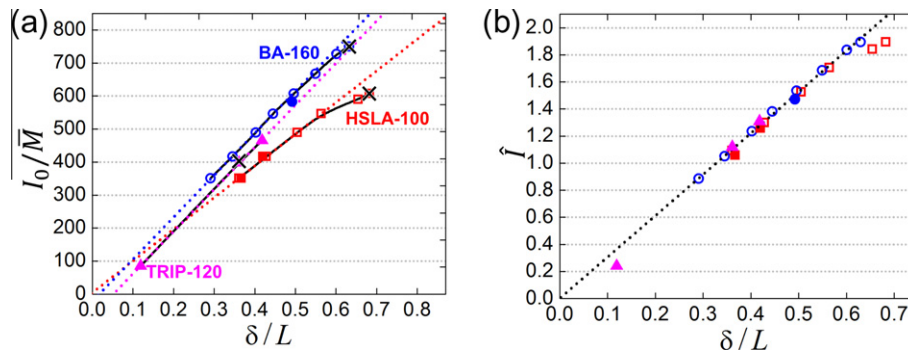
Fig. 14. Comparison of alloy performance. (a) Impulse per areal mass vs. normalized deflection curves for three alloys obtained from experiments (solid symbols) and numerical simulations (hollow symbols). Onset of panel failure is indicated by a cross symbol. Linear fitting was performed on each alloy (dashed lines) before failure. (b) Plot of non-dimensional impulse vs. normalized deflection responses for all three alloys, which collapse into a single linear relationship (dashed line) before extensive damage and failure.

6. Ductility improvement in TRIP-120

### 6.1. Ductility improvement by applying a two-step heat treatment

TRIP-120 was originally designed for a single step temper of 750 °C for 10 h, which gave rise to a cellular reaction occurring at the grain boundaries with the formation of the equilibrium η phase as opposed to the desired metastable γ' precipitates. The η phase precipitates are coarse platelets and create a lamellar structure starting at the grain boundaries as shown in Fig. 15. As revealed by the FSI experiments here reported, this cellular reaction limits the ductility of TRIP-120 (Kotval and Hatwell, 1969), which fails prematurely by intergranular fracture. As a result, a heat treatment optimization study has been carried out to determine the proper processing steps that eliminate the cellular reaction from occurring at the grain boundaries and maximize the fracture ductility. The challenge is to precipitate out the metastable γ' phase to achieve the strength goal of 120 ksi and the proper austenite stability without formation of the equilibrium η phase. Cellular reactions require precipitation and concurrent grain boundary migration (Manna and Gust, 2001). Thus, cellular reactions can be eliminated if the grain boundaries are sufficiently pinned. The concept is to develop a two-step heat treatment: the first step locks the grain boundaries with discrete γ' particles and the second step precipitates out the remaining γ' particles to achieve the desired strength. In a reference work, a similar heat treatment was successfully applied to a Cu–Ni–Al system to eliminate an undesired cellular reaction (Tsuda and Nakayam, 1986).

In the TRIP-120 system, the equilibrium γ' phase fraction decreases with increasing tempering temperature, but the precipitation rate kinetics increase. The γ' phase fraction drops to 0 at a metastable solvus temperature of 855 °C, and tempering at 800 °C or above leads to rapid formation of the η phase. Thus, our first step in the multi-step heat treatment was constrained to 775 °C. Samples were tempered at 775 °C for different times followed by Vickers microhardness measurements and optical microscopy to monitor γ' and η precipitation. The first step in the heat treatment was then selected as 775 °C for 2 hours, corresponding to the maximum strength increment that can be achieved before the η phase forms.

While the first step precipitates discrete γ' particles to lock in the grain boundaries, the second step aims to precipitate out more γ' particles at a lower temperature to reach the appropriate strength and austenite stability. For the second aging step, samples were tempered at 725 °C for different times. Once again Vickers microhardness measurements were made and optical microscopy was carried out to monitor γ' and η precipitation. The peak hardness condition that eliminates formation of grain boundary lamellar structures is achieved with a two-step temper: 775 °C 2 h, 725 °C 2 h. After the two-step temper, TRIP-120 has more than doubled its hardness (from 172 VHN to 376 VHN), and the cellular grain boundary reaction has been eliminated. Fig. 15 shows the difference in microstructures for TRIP-120 tempered for 10 h at 750 °C in comparison to TRIP-120 after the two-step temper.

By eliminating the cellular reaction from the grain boundaries, TRIP-120 shows an improvement in fracture ductility for the
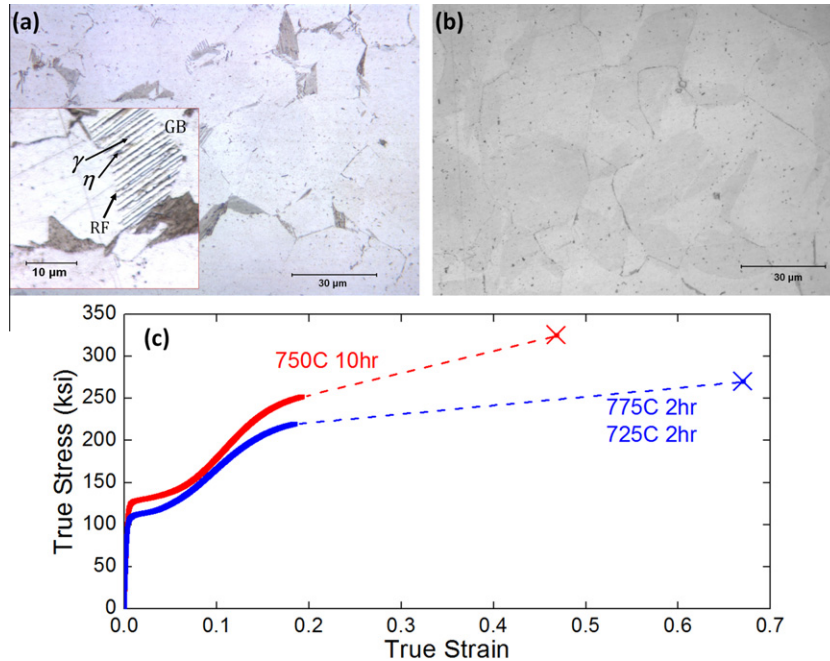
Fig. 15. (a) Optical microscopy showing the microstructure in TRIP-120 after tempering at 750 °C, for 10 h showing a cellular reaction occurring at the grain boundary; (b) optical micrograph of TRIP-120 tempered at 775 °C for 2 h, and at 725 °C for 2 h with no cellular reaction (dark regions) at grain boundaries; (c) quasi-static true stress-true strain results for TRIP-120 comparing the performance of the single step temper to the two-step temper.

two-step temper, Fig. 15c, with a true fracture strain of 67% as opposed to 47% seen in the single step temper. The uniform ductility of the alloy remains approximately 20%.

### 6.2. Ductility improvement from warm working

Although the two-step temper showed some improvement in the fracture strain, the strength level and strain-hardening decreased. In an effort to drastically improve the fracture strain, we explored warm-working TRIP-120 to 23% and 36% area reductions at 450 °C, which has given improved tensile properties for EX425 – a similar, fully austenitic steel (Stavehaug, 1990). The temperature of 450 °C was selected in order to be above the M_d temperature to prevent transformation of the austenitic matrix. Likewise, the temperature is low enough to suppress dislocation recovery because the warm working processing is intended to introduce forest dislocations into the matrix that would increase hardening. After warm working, TRIP-120 can be tempered at lower temperatures for shorter times to achieve the desired strength goal and prevent the occurrence of cellular reaction. This processing step catalyzes intragranular precipitation by creating heterogeneous sites of γ' precipitation, which in turn avoids η formation at the grain boundaries.

Warm working alters the dislocation density, the stability of the parent phase, and the tempering conditions to achieve peak hardness. In order to find optimal tempering conditions, an isochronal tempering study was completed, measuring the Vicker's microhardness for TRIP-120 heat treated between the temperature range of 600 °C and 750 °C for 1 h and 8 h as shown in Fig. 16. For 8 h tempers, peak hardness occurs at 700 °C for the 23% and 36% warm worked conditions. For 1 h tempers, peak hardness occurs at 725 °C for the 23% and 36% warm worked conditions.

With an understanding of the relationship between tempering conditions and hardness, room temperature quasi-static tension tests were performed for TRIP-120 treated with various conditions. For the 36% warm worked tempered at 700 °C for 1 h, TRIP-120 exhibits a yield strength of 180 ksi, a uniform ductility of 33%,
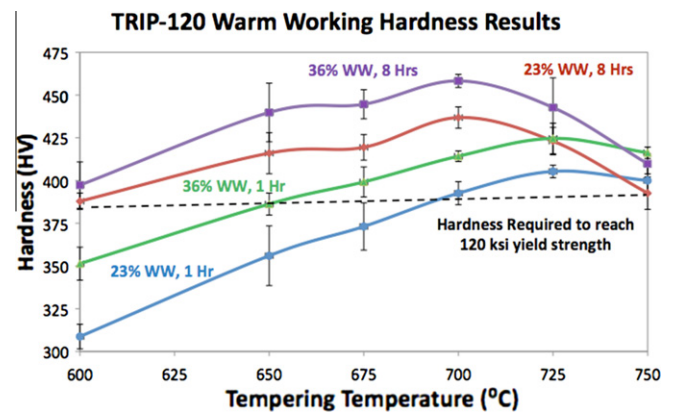
Fig. 16. Isochronal study of Vickers microhardness for warm worked TRIP-120 over the temperature range of 600–750 °C for 1 and 8 h.
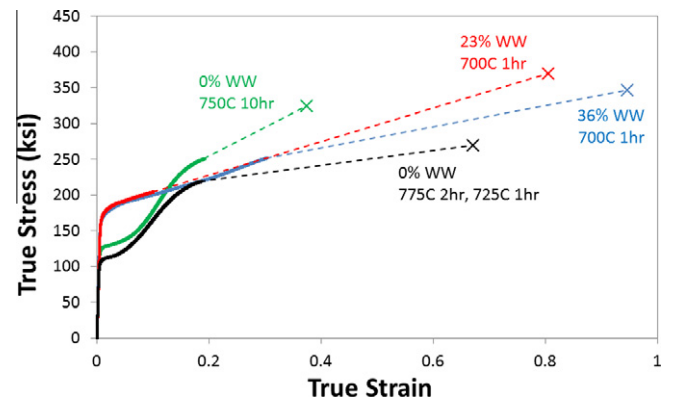
Fig. 17. Quasi-static tension tests that summarize the best results from single step heat treatments, two-step heat treatments, 23% warm worked condition, and 36% warm worked condition of TRIP-120.
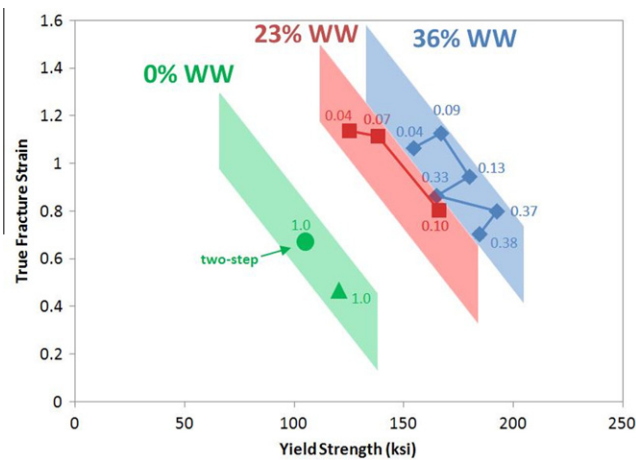
Fig. 18. True fracture strain vs. yield strength plotted for TRIP-120 under various levels of warm working. Colored bands for various levels of warm work illustrate the strength and fracture strain combinations that can be achieved. Each data point is labeled with a kinetic parameter that quantifies the aging condition relative to the condition of peak hardness.

and a true fracture strain of 95%, approximately a 50% improvement in yield strength and uniform ductility and 100% improvement in fracture strain in comparison to the original single step temper (Fig. 17).

The results of warm working have led to increased strength and fracture strain values as shown graphically in Fig. 18. Bands illustrate the strength and fracture strain combinations that can be achieved for a given level of warm working. Each data point is labeled with a kinetic parameter that quantifies degree of aging relative to the condition of peak hardness, where a value of 1.0 refers to the peak hardness condition. With increased aging, the yield strength increases and the fracture strain decreases along the bands. In summary, by utilizing warm working, it is possible to precipitate out γ' at lower temperatures for shorter times to avoid the formation of the η phase at the grain boundaries and achieve fracture strains greater than 110%. Further testing will explore the dynamic behavior of these promising materials.

7. Concluding remarks

The performance of monolithic steel panels subjected to underwater impulsive loads was investigated. Two martensitic high strength steel alloys, HSLA-100 and BA-160, and one fully austenitic alloy, TRIP-120, were evaluated. Material design based on deformation modes elicited in structures subjected to blast loading was presented for both martensitic and austenitic steels. Then, an experimental–computational methodology based on dynamic high strain rate experiments, fluid–structure experiments, and modeling of fluid–structure interaction and material ductile failure was presented. The approach provided insight into the relationships between material properties (strength, uniform ductility, and post-necking ductility) and blast resistance of structures. In particular, it allowed identification of material/structure performances by identifying impulse-center deflection behavior and the impulse leading to panel fracture.

Among the investigated steel alloys, BA-160 is currently the best material to sustain underwater impulsive loadings, since it shows failure at an impulse per areal mass 25% higher than that of HSLA-100. Moreover, BA-160 is also an excellent material choice for structures where minimal deflections are desired. There is one aspect that needs further investigation concerning the performance of this martensitic steel, which is assessing the impact of limited uniform ductility in full scale structures. After necking,

strain localization develops within a limited region in the panel, which leads to fracture. Hence, the localization regime in the FSI experiments, unlike the uniform deformation regime, will only scale up with the thickness dimension based on the recent study by Nielsen and Hutchinson (2011). This feature points back to the benefits of the austenitic TRIP-120 steel alloy, which was designed to delay necking (i.e., increase uniform ductility). Even when the alloy failed at relatively low impulses, compared to martensitic steel alloys, we presented two promising strategies, multi-step tempering and warm working, for improving its performance by suppressing microcracking through elimination of grain boundary cellular reactions.

References

Asgari, S., 2001. Structure and strain hardening of superalloy AEREX350. Journal of Materials Processing Technology 118, 246–250.

Ashani, J.Z., Ghamsari, A.K., 2007. Theoretical and experimental analysis of plastic response of isotropic circular plates subjected to underwater explosion loading. In: International Conference on Advanced Computational Engineering and Experimenting. Wiley-VCH Verlag Gmbh, Algarve, Portugal, pp. 171–175.

Cole, R.H., 1948. Underwater Explosions. Princeton University Press.

Czyryca, E.J. et al., 1990a. Development and certification of HSLA-100 steel for naval ship construction. Naval Engineers Journal 102, 63–82.

Czyryca, E.J. et al., 1990b. Development and certification of HSLA-100 steel for naval ship construction-reply. Naval Engineers Journal 102, 103–104.

Czyryca, E.J. et al., 1990c. Development and certification of HSLA-100 steel for naval ship construction-reply. Naval Engineers Journal 102, 104.

Das, S.K. et al., 2006. The effect of variation of microstructure on fracture mechanics parameters of HSLA-100 steel. Materials Science and Engineering A-Structural Materials Properties Microstructure and Processing 431, 68–79.

Densley, J.M., Hirth, J.P., 1998. Mixed mode fracture of an HSLA-100 steel. Scripta Materialia 39, 881–885.

Deshpande, V.S., Fleck, N.A., 2005. One-dimensional response of sandwich plates to underwater shock loading. Journal of the Mechanics and Physics of Solids 53, 2347–2383.

Dhua, S.K. et al., 2003. Effect of cooling rate on the As-quenched microstructure and mechanical properties of HSLA-100 steel plates. Metallurgical and Materials Transactions A-Physical Metallurgy and Materials Science 34A, 2493–2504.

Dunne, D.P. et al., 1996. Isothermal transformation products in a Cu-bearing high strength low alloy steel. ISIJ International 36, 324–333.

Espinosa, H. et al., 2006. A novel fluid–structure interaction experiment to investigate deformation of structural elements subjected to impulsive loading. Experimental Mechanics 46, 805–824.

Florence, A.L., 1966. Circular plate under a uniformly distributed impulse. International Journal of Solids and Structures 2, 37–40, IN31–IN32, 41–47.

Goodman, S.R. et al., 1973. FIM-atom probe study of precipitation of copper from iron-1.4 at Pct copper. 1. Field-ion microscopy. Metallurgical Transactions 4, 2363–2369.

Gurson, A., 1977. Continuum theory of ductile rupture by void nucleation and growth: Part I – yield criteria and flow rules for porous ductile media. Journal of Engineering Materials and Technology 99, 2–15.

Haidemenopoulos, G., 1988. Dispersed-phase transformation toughening in ultrahigh-strength steels. Ph.D. thesis, Massachusetts Institute of Technology.

Hutchinson, J., Neale, K., 1978. Sheet necking-II. Time-independent behavior. Mechanics of Sheet Metal Forming, 127–153.

Hutchinson, J.W., Xue, Z.Y., 2005. Metal sandwich plates optimized for pressure impulses. International Journal of Mechanical Sciences 47, 545–569.

Irvine, K.J., Pickering, F.B., 1963. Low-carbon steels with ferrite–pearlite structures. Journal of the Iron and Steel Institute 201, 944–960.

Jones, N., 1989. Structural Impact. Cambridge University Press.

Kotval, P., Hatwell, H., 1969. Discontinuous precipitation of $M_{23}C_6$ carbide in a nickelbase superalloy. Transactions of the American Institute of Mining, Metallorgical and Petroleum Engineers 245, 1821–1823.

Latourte, F. et al., 2010. Shear and tensile plastic behavior of austenitic steel TRIP-120 compared with martensitic steel HSLA-100. International Journal of Fracture, 1–18.

Latourte, F., Grégoire, D., Zenkert, D., Espinosa, H.D., 2011. Failure mechanisms in monolithic and sandwich composite panels subjected to underwater impulsive loads. Journal of the Mechanics and Physics of Solids.

Leal, R.H., 1984. Transformation Toughening of Metastable Austenitic Steels. Massachusetts Institute of Technology.

Liang, Y. et al., 2007. The response of metallic sandwich panels to water blast. Journal of Applied Mechanics 74, 81–99.

Manna, I., Pabi, S.K., Gust, W., 2001. Discontinuous reactions in solids. International Materials Reviews 46, 53–90.

Martineau, R.L. et al., 2004. Penetration of HSLA-100 steel with tungsten carbide spheres at striking velocities between 0.8 and 2.5 km/s. International Journal of Impact Engineering 30, 505–520.

McCarren, M. et al., March 2004. BlasTruss: Civil Shield Technologies, IDEA. Northwestern University.

Mckenna, A. et al., 2007. IDEA: formalizing the foundation for an engineering design education. International Journal of Engineering Education 22, 671.

Mori, L.F. et al., 2007. Deformation and fracture modes of sandwich structures subjected to underwater impulsive loads. Journal of Mechanics of Materials and Structures 2, 1981–2006.

Mori, L.F. et al., 2009. Deformation and failure modes of I – core sandwich structures subjected to underwater impulsive loads. Experimental Mechanics 49, 257–275.

Nahshon, K., Hutchinson, J., 2008. Modification of the Gurson model for shear failure. European Journal of Mechanics-A/Solids 27, 1–17.

Neuberger, A. et al., 2007. Scaling the response of circular plates subjected to large and close-range spherical explosions. Part I: Air-blast loading. International Journal of Impact Engineering 34, 859–873.

Nichols, D.C., 1990. Development and certification of HSLA-100 steel for naval ship construction-comment. Naval Engineers Journal 102, 102–103.

Nielsen, K.L., Hutchinson, J.W., 2011. Cohesive traction-separation laws for tearing of ductile metal plates. International Journal of Impact Engineering.

Nurick, G.N., Martin, J.B., 1989a. Deformation of thin plates subjected to impulsive loading. A review, Part I: theoretical consideration. International Journal of Impact Engineering 8 (2), 151–170.

Nurick, G.N., Martin, J.B., 1989b. Deformation of thin plates subjected to impulsive loading. A review, Part II: experimental studies. International Journal of Impact Engineering 8 (2), 171–186.

Nurick, G.N., Shave, G.C., 1996. The deformation and tearing of thin square plates subjected to impulsive loads – an experimental study. International Journal of Impact Engineering 18, 99–116.

Nurick, G.N. et al., 1996. Tearing of blast loaded plates with clamped boundary conditions. International Journal of Impact Engineering 18, 803–827.

Olson, G., 1996. Transformation plasticity and toughening. Le Journal de Physique IV 6, 1.

Qiu, X. et al., 2004. Dynamic response of a clamped circular sandwich plate subject to shock loading. Journal of Applied Mechanics-Transactions of the ASME 71, 637–645.

Rajendran, R., Narashimhan, K., 2001. Performance evaluation of HSLA steel subjected to underwater explosion. Journal of Materials Engineering and Performance 10, 66–74.

Rajendran, R., Narasimhan, K., 2006. Deformation and fracture behaviour of plate specimens subjected to underwater explosion – a review. International Journal of Impact Engineering 32, 1945–1963.

Rittel, D. et al., 2006. Adiabatic shear failure and dynamic stored energy of cold work. Physical Review Letters 96, 75502.

Rittel, D. et al., 2008. Dynamic recrystallization as a potential cause for adiabatic shear failure. Physical Review Letters 101, 165501.

Russell, K., Brown, L., 1972. A dispersion strengthening model based on differing elastic moduli applied to the iron–copper system. Acta Metallurgica 20, 969–974.

Sadhukhan, P., 2008. Computational Design and Analysis of High Strength Austenitic TRIP Steels for Blast Protection Applications. Northwestern University.

Saha, A., 2004. Systems Design of ultra-tough high-strength Steels for blast-resistant Naval Hull Application. Northwestern University.

Saha, A., Olson, G.B., 2007. Computer-aided design of transformation toughened blast resistant naval hull steels: Part I. Journal of Computer-Aided Materials Design 14, 177–200.

Saha, A. et al., 2007. Prototype evaluation of transformation toughened blast resistant naval hull steels: Part II. Journal of Computer-Aided Materials Design 14, 201–233.

Sawhill, J.M., 1990. Development and certification of HSLA-100 steel for naval ship construction-comment. Naval Engineers Journal 102, 103.

Stavehaug, F., 1990. Transformation Toughening of γ' strengthened Metastable Austenitic Steels. Department of Materials Science and Engineering, Massachusetts Institute of Technology.

Symonds, P.S., Wierzbicki, T., 1979. Membrane mode solutions for impulsively loaded circular plates. Journal Of Applied Mechanics-Transactions Of The ASME 46, 58–64.

Taylor, G.I., 1963. The Scientific Papers of G.I. Taylor. Cambridge University Press, Cambridge, pp. 287–303.

Teeling-Smith, R.G., Nurick, G.N., 1991. The deformation and tearing of thin circular plates subjected to impulsive loads. International Journal of Impact Engineering 11, 77–91.

Tsuda, H.I.T., Nakayam, Y., 1986. The improvement of microstructures and mechanical properties in Cu–Ni–Al alloys by two-step ageing. Scripta Metallurgica 20, 1555–1559.

Tvergaard, V., 1990. Material failure by void growth to coalescence. Advances in Applied Mechanics 27, 83–151.

Vaynman, S. et al., 2008. High-strength low-carbon ferritic steel containing Cu–Fe–Ni–Al–Mn precipitates. Metallurgical and Materials Transactions A-Physical Metallurgy and Materials Science 39A, 363–373.

Vaziri, A., 2007. Performance and failure of metal sandwich plates subject to shock loading. Journal Of Mechanics Of Materials And Structures 2, 1947–1963.

Wierzbicky, T., 1969. Large deflections of a strain rate sensitive plate loaded impulsively. Archiwum Mechaniki Stosowanej 21, 67.

Wise, J., 1998. Systems Design of Advanced Gear Steels. Northwestern University.

Wojno, W., Wierzbicki, T., 1980. Perturbation solution for impulsively loaded visco-plastic plates. International Journal of Non-Linear Mechanics 15, 211–223.

Xue, Z.Y., Hutchinson, J.W., 2003. Preliminary assessment of sandwich plates subject to blast loads. International Journal of Mechanical Sciences 45, 687–705.

Xue, Z., Hutchinson, J., 2004. A comparative study of impulse-resistant metal sandwich plates. International Journal of Impact Engineering 30, 1283–1305.

Xue, Z., 2010. Calibration procedures for a computational model of ductile fracture. Engineering Fracture Mechanics 77, 492–509.